

Linear paired electrochemical valorization of glycerol enabled by the electro-Fenton process using a stable NiSe₂ cathode

Hongyuan Sheng, Aurora N. Janes, R. Dominic Ross, Heike Hofstetter, Kwanpyung Lee, J. R. Schmidt, and Song Jin**

Department of Chemistry, University of Wisconsin–Madison, 1101 University Avenue, Madison, Wisconsin 53706, United States

*Corresponding author emails: schmidt@chem.wisc.edu; jin@chem.wisc.edu

ABSTRACT

Electrochemical valorization of surplus biomass-derived feedstocks such as glycerol into high-value chemicals offers a sustainable route for utilizing biomass resources and decarbonizing chemical manufacturing; however, glycerol is typically valorized solely via anodic oxidation, with lower-value products such as hydrogen gas generated at cathode. Here, we establish the efficient cathodic valorization of glycerol to the desirable C₃ oxidation products via the electro-Fenton process at a stable NiSe₂ cathode, built upon the theoretical understanding and experimental demonstration of NiSe₂’s high selectivity and stability toward acidic H₂O₂ electrosynthesis. A proof-of-concept linear paired electrochemical process for concurrently valorizing glycerol into the same oxidation products at both NiSe₂ cathode and Pt anode achieves high selectivity for value-added C₃ products and high glycerol conversion with little external energy input needed, when the electro-Fenton generation of hydroxyl radicals is carefully controlled. This conceptual strategy of linear pairing is generalizable for enabling atom-efficient electro-refinery of diverse biomass-derived feedstocks.

Harnessing solar and wind generated electricity for electrochemical synthesis of high-value chemicals from biomass feedstocks offers a sustainable alternative to conventional chemical manufacturing from fossil fuels¹⁻³. Glycerol is a byproduct of the rapidly growing biodiesel production and has become a surplus biomass-derived chemical⁴ with a low price of 0.17 \$/kg⁵. Oxidative upgrading of glycerol is very attractive⁶⁻⁸, because all C₃ and C₂ oxidation products have higher economic values than glycerol⁷⁻⁹. Compared to thermal oxidation that requires high temperature and oxygen pressure, electrochemical oxidation⁹ poses several advantages including near-ambient operation, less reagent waste, and distributed small-scale production^{3,8}.

Electrochemical oxidation of glycerol typically occurs at catalytic anodes made of noble metals¹⁰⁻¹³ or earth-abundant electrocatalysts¹⁴⁻¹⁶, which is paired with either four-electron oxygen reduction reaction (4e⁻ ORR) in a galvanic cell^{9,17} or hydrogen evolution reaction (HER) in an electrolytic cell^{9,18} (Fig. 1a). In either case, the chemicals generated at cathode have lower economic values (e.g., ~1 \$/kg or ~0.002 \$/mol for H₂ from steam methane reforming¹⁹) than the glycerol-derived chemicals generated at anode [e.g., ~150 \$/kg or ~13.5 \$/mol for dihydroxyacetone (DHA)^{7,20}]. Recently, anodic glycerol oxidation has been paired with CO₂²¹ or CO²² reduction reaction (CO₂/CORR) that generates C₁ and/or C₂₊ products at cathode²³ (Fig. 1a), but the different cathode and anode feeds lead to different product portfolios between the two half-cells with additional system complexity and separation cost. Using glycerol as the sole feed in a so-called linear paired electrochemical process^{3,24-26} to produce the same value-added oxidation products at both cathode and anode simultaneously could be appealing.

Linear paired electrochemical valorization of glycerol requires a cathodic reaction that can generate oxidative species to oxidize glycerol. Hydrogen peroxide (H₂O₂) is an oxidant (E° =

1.76 V vs. SHE) that can be cathodically generated via the selective $2e^-$ ORR ($O_2 + 2 H^+ + 2 e^- \rightarrow H_2O_2$)^{27,28}, and be further converted into the even more oxidizing hydroxyl radical ($\cdot OH$, $E^\circ = 2.80$ V vs. SHE) by the Fe^{2+} -mediated electro-Fenton process in acidic solutions ($Fe^{2+} + H_2O_2 + H^+ \rightarrow Fe^{3+} + H_2O + \cdot OH$) where Fe^{2+} is regenerated at the H_2O_2 -generating cathode ($Fe^{3+} + e^- \rightarrow Fe^{2+}$)²⁹. The application of electro-Fenton process has been largely limited to environmental pollutant removal²⁹, but chemically generated $\cdot OH$ from H_2O_2 has found use in biomass-to-chemical processes³⁰ such as carbohydrate oxidation^{31,32} and lignin depolymerization³³. These works suggest it might be possible to utilize electro-Fenton process for electrochemical oxidation of glycerol to value-added C_3 (and C_2) products when the $\cdot OH$ electrogeneration can be carefully controlled. However, robust, inexpensive, and selective $2e^-$ ORR electrocatalysts to produce H_2O_2 under slightly acidic conditions are needed for enabling efficient electro-Fenton process.

Here, we present the systematic investigation of cathodic valorization of glycerol via the electro-Fenton process, and the further linear pairing with the anodic oxidation to concurrently produce the same glycerol-derived oxidation products at both cathode and anode (Fig. 1b). This is made possible by the discovery of a robust and earth-abundant $NiSe_2$ electrocatalyst for the selective $2e^-$ ORR and electro-Fenton process in acidic solutions. Building on the recent developments of transition metal compounds^{34,35} as selective $2e^-$ ORR catalysts that are more cost-effective than noble metals³⁶ and more catalytically active than carbon-based materials in acidic solutions³⁷, we combine theory and experiment to elucidate the origins of $NiSe_2$'s high selectivity toward acidic $2e^-$ ORR and excellent stability against surface oxidative leaching. $NiSe_2$ cathode operated at the optimum potential for H_2O_2 electrosynthesis and electro-Fenton process enables the efficient glycerol oxidation in the cathodic half-cell, with a high glycerol conversion and high selectivity for valuable C_3 products. Finally, a linear paired electrochemical

system comprising of NiSe_2 cathode and Pt anode for efficient concurrent glycerol valorization to C_3 products is demonstrated under a marginal external applied bias.

RESULTS

Identifying $c\text{-NiSe}_2$ catalyst for the electro-Fenton process

The Fe^{2+} -mediated electro-Fenton process operates at an optimum pH of ~ 3 (ref. ²⁹) and poses more stringent requirements for catalyst stability than 2e^- ORR because $\cdot\text{OH}$ is more oxidizing than H_2O_2 . Therefore, an electrocatalyst that is not only selective for acidic 2e^- ORR but also stable in the presence of strong oxidants such as H_2O_2 and $\cdot\text{OH}$ is needed. We utilized the calculated bulk Pourbaix diagrams available from the Materials Project³⁸ to identify promising earth-abundant catalyst candidates with high aqueous electrochemical stability in the pH and potential ranges of interest for acidic 2e^- ORR. Similar to cubic pyrite-type CoSe_2 ($c\text{-CoSe}_2$, Fig. 2a), an acidic 2e^- ORR catalyst with demonstrated stability³⁵, cubic NiSe_2 ($c\text{-NiSe}_2$, Fig. 2a) exhibits a wide electrochemical stability window in the bulk Pourbaix diagram (Supplementary Fig. 1). Therefore, NiSe_2 could be a promising cathode catalyst for the electro-Fenton process.

The promise of $c\text{-NiSe}_2$ as an active and selective 2e^- ORR catalyst is revealed by the calculated free energy diagrams of the ORR energetics on the most thermodynamically stable (100) surface (Fig. 2b). The 2e^- ORR (Fig. 2b, solid traces) proceeds via the adsorption of OOH^* ($\text{O}_{2(\text{g})} + * + \text{H}^+ + \text{e}^- \rightarrow \text{OOH}^*$, where $*$ is the unoccupied surface binding site) followed by its desorption to form H_2O_2 ($\text{OOH}^* + \text{H}^+ + \text{e}^- \rightarrow \text{H}_2\text{O}_{2(\text{aq})} + *$). At the calculated standard equilibrium potential of 2e^- ORR (U_{RHE}^0), the preferential binding of OOH^* to the Ni site on $c\text{-NiSe}_2$ is relatively weak (endothermic by 0.10 eV), whereas the Co site on $c\text{-CoSe}_2$ preferentially

binds to OOH^* more strongly (exothermic by 0.24 eV)³⁵. Thus, *c*-NiSe₂ is expected to be not only active for 2e⁻ ORR as the OOH^* adsorption is nearly thermoneutral at U_{RHE}^0 , but also selective toward 2e⁻ (vs. 4e⁻) ORR because it is situated on the weak OOH^* binding leg of the 2e⁻ ORR volcano³⁶. In contrast, *c*-CoSe₂ is situated on the strong OOH^* binding leg. Furthermore, the 2e⁻ ORR selectivity is also kinetically governed by the resistance to the O-O bond cleavage in OOH^* , which leads to the competing 4e⁻ ORR (Fig. 2b, dashed traces). We reason that the OOH^* dissociation on pyrite-type structures likely proceeds via a dinuclear pathway across two neighboring metal sites ($\text{OOH}^* + * \rightarrow \text{O}^* + \text{OH}^*$)³⁴. But this pathway features a high activation barrier of 0.61 eV (0.63 eV) on *c*-NiSe₂ (*c*-CoSe₂) and is kinetically disfavored due to the large spacing between the neighboring metal sites separated by diselenide anions. Thus, computational assessments of ORR pathways suggest that *c*-NiSe₂ should be active and selective for 2e⁻ ORR.

The surface stability of *c*-NiSe₂ under aqueous electrochemical environments is evaluated by considering O* and/or OH* adsorbate formation when the surface is in equilibrium with water. Unlike *c*-CoSe₂ where O* and OH* preferentially bind to Se (Se-O*) and Co (Co-OH*), respectively, Ni on *c*-NiSe₂ is the preferential binding site for both O* (Ni-O*) and OH* (Ni-OH*). On a surface unit cell comprising of two metal sites and four Se sites, should O* builds up on the *c*-NiSe₂ surface, a significant O* coverage would have to be reached (which is unlikely because O* binds to Ni endothermically by 0.08 eV at U_{RHE}^0) before any O* would bind to Se; however, any presence of O* on *c*-CoSe₂ would bind to Se immediately (Fig. 2c). Since one possible degradation pathway of pyrite-type structures is the oxidation of dichalcogenide anions followed by the dissolution of metal cations (Supplementary Fig. 1), the low affinity of O* to Se on *c*-NiSe₂ suggests an increased resistance to surface oxidation. In addition, OH* binds to Ni more weakly (endothermic by 0.27 eV) than to Co (exothermic by 0.08 eV) at U_{RHE}^0 , which

allows the *c*-NiSe₂ surface to stay clean and mostly free of adsorbate over a wider range of potentials compared to the *c*-CoSe₂ surface (Fig. 2c). Note that O* and OH* can also form during ORR if the O-O bond cleavage occurs (Fig. 2b). Therefore, these surface adsorbate analyses suggest *c*-NiSe₂ should be more resistant to surface oxidation and degradation under aqueous environments and ORR operating conditions.

Electrocatalytic 2e⁻ ORR properties and stability of *c*-NiSe₂

We synthesized nanostructured *c*-NiSe₂ (Supplementary Fig. 2) via a hydrothermal method, and examined the acidic 2e⁻ ORR catalytic properties of the powder sample by drop-casting on a rotating ring-disk electrode (RRDE) (see Methods for details). We also synthesized nanostructured *c*-CoSe₂ catalyst³⁵ as a comparison (Supplementary Fig. 3). RRDE experiments were performed with various catalyst loadings that resulted in similar ranges of double-layer capacitances (C_{dl}) between these two catalysts (Supplementary Fig. 4) for fair comparisons. In O₂-saturated 0.05 M H₂SO₄ (pH ~1.2), *c*-NiSe₂ exhibits high H₂O₂ selectivity (up to 95%) and relatively little dependence on overpotential and catalyst loading (Fig. 3a and 3b). In contrast, although *c*-CoSe₂ is more catalytically active toward 2e⁻ ORR, the H₂O₂ selectivity decreases more dramatically with increasing overpotential and catalyst loading (Fig. 3a and 3b). Such differences between the H₂O₂ selectivity profiles of *c*-NiSe₂ and *c*-CoSe₂ are also observed at pH ~2.8 in O₂-saturated 0.1 M NaHSO₄/Na₂SO₄ buffer (Supplementary Fig. 5 and 6), further showing that *c*-NiSe₂ is more selective toward acidic 2e⁻ ORR than *c*-CoSe₂.

The stability of *c*-NiSe₂ (vs. *c*-CoSe₂) catalyst for acidic 2e⁻ ORR was evaluated by long-term RRDE stability tests at various catalyst loadings. The catalyst stability is monitored by tracking the disk potential at a certain disk current density (j_{disk}) or peroxide current density ($j_{peroxide}$) (Supplementary Fig. 7). The stable disk potential throughout the tests shows that *c*-

NiSe_2 exhibits a higher catalyst stability than $c\text{-CoSe}_2$ at both pH ~ 1.2 (0.05 M H_2SO_4) and pH ~ 2.8 (0.1 M $\text{NaHSO}_4/\text{Na}_2\text{SO}_4$) (Supplementary Fig. 8 and 9). The spent catalysts show no obvious structural and compositional change (Supplementary Fig. 10). We further performed elemental analyses of the spent electrolytes to quantify the leaching rates of metal and selenium from the catalysts normalized by the catalyst masses ($\mu\text{mol g}_{\text{catalyst}}^{-1} \text{h}^{-1}$). The ratio between the Co and Se leaching rates of the less stable $c\text{-CoSe}_2$ is close to the 1:2 stoichiometry (Fig. 3c and Supplementary Table 1). This suggests the leaching of $c\text{-CoSe}_2$ could be initiated by the surface oxidation of Se_2^{2-} to the soluble SeO_x due to the preferential affinity of O^* to its Se site (Fig. 2c), followed by the near-stoichiometric dissolution of Co^{2+} from the surface. In contrast, the Se leaching from the more stable $c\text{-NiSe}_2$ is not only substantially suppressed compared to $c\text{-CoSe}_2$, but also slower than the Ni leaching (Fig. 3c). These suggest the leaching of $c\text{-NiSe}_2$ could mainly result from the preferential adsorption of both O^* and OH^* onto Ni (Fig. 2c) and the subsequent acid-base reaction with the electrolyte to dissolve Ni^{2+} . This hypothesis is supported by the slower leaching of $c\text{-NiSe}_2$ under the less acidic pH of ~ 2.8 (Fig. 3c), and future studies will be helpful for confirming the catalyst leaching mechanisms. These in-depth catalyst leaching studies further confirm the enhanced stability of $c\text{-NiSe}_2$ for acidic 2e^- ORR.

Bulk electrosynthesis of H_2O_2 using $c\text{-NiSe}_2$ cathode

We further performed constant-potential bulk electrosynthesis using integrated electrodes of $c\text{-NiSe}_2$ nanosheets directly grown on carbon fiber paper (NiSe_2/CFP , Supplementary Fig. 11) to accumulate H_2O_2 in O_2 -saturated 0.05 M H_2SO_4 in a two-compartment three-electrode H-cell (Supplementary Fig. 12) at various applied potentials ranging from 0.50 to 0.65 V vs. RHE (Fig. 3d and Supplementary Fig. 13). Both the cumulative H_2O_2 yield and selectivity after 6 hours of bulk electrosynthesis are potential-dependent, and peak at the optimum potential of 0.60 V vs.

RHE (Fig. 3d). Cyclic voltammograms recorded before and after each electrosynthesis trial suggest additional cathodic current is generated on NiSe_2/CFP after the accumulation of H_2O_2 in the solution (Supplementary Fig. 13), likely due to the electroreduction of H_2O_2 to water as the Faradaic side reaction.

To understand this potential-dependent electrosynthesis of H_2O_2 , we studied the side reaction of H_2O_2 electroreduction in competition with 2e^- ORR on $c\text{-NiSe}_2$ catalyst drop-casted on RRDE. In 0.05 M H_2SO_4 , the catalytic onset potential of H_2O_2 electroreduction on $c\text{-NiSe}_2$ coincides with that of 2e^- ORR, and the rate of H_2O_2 electroreduction increases with higher overpotential and H_2O_2 concentration (Supplementary Fig. 14a). Therefore, as H_2O_2 concentration builds up, the net rate of H_2O_2 production (i.e., the production rate minus the electroreduction rate of H_2O_2) on $c\text{-NiSe}_2$ is positive only in a certain potential range and displays a parabolic trend peaking at an optimum potential (Supplementary Fig. 14b). Similarly, H_2O_2 electroreduction also occurs on $c\text{-CoSe}_2$ but it affects the net production rate less because $c\text{-CoSe}_2$ exhibits a more positive catalytic onset potential for 2e^- ORR (Supplementary Fig. 14 and Fig. 3a). A similar parabolic trend in the net rate of H_2O_2 production on $c\text{-NiSe}_2$ is observed in 0.1 M $\text{NaHSO}_4/\text{Na}_2\text{SO}_4$ buffer at pH ~2.8 (Supplementary Fig. 15). These results show the importance of considering H_2O_2 electroreduction and operating NiSe_2/CFP at the optimum applied potential for H_2O_2 electrosynthesis.

We demonstrated sustained bulk electrosynthesis of H_2O_2 in O_2 -saturated 0.05 M H_2SO_4 at the optimum 0.60 V vs. RHE using one NiSe_2/CFP electrode repeatedly for five consecutive runs over 37 hours (Fig. 3e). Since the cathodic current on NiSe_2/CFP gradually increased over time because of the electroreduction of the accumulated H_2O_2 , we replaced the catholyte with fresh H_2O_2 -free electrolyte between runs to maintain the steady net production of H_2O_2 .

(Supplementary Fig. 16). Over the initial 2-hour period of each run, the NiSe₂/CFP electrode consistently accumulated 203 ± 10 ppm H₂O₂ and produced 15.4 ± 1.4 μ mol H₂O₂ with a cumulative H₂O₂ selectivity of $51.8 \pm 1.8\%$ with no obvious decay (Fig. 3e and Supplementary Fig. 16). A higher H₂O₂ yield of 34.8 ± 2.8 μ mol and a higher accumulated concentration of 661 ± 53 ppm were achieved over a longer period of 7.4 ± 0.5 hours at the end of each run, but with a lower H₂O₂ selectivity of $30.8 \pm 1.2\%$ (Fig. 3e and Supplementary Fig. 16). NiSe₂/CFP shows a similar H₂O₂ electrosynthesis performance in O₂-saturated 0.1 M NaHSO₄/Na₂SO₄ buffer at pH ~ 2.8 (Supplementary Fig. 17). The spent NiSe₂/CFP electrode is structurally and compositionally stable after H₂O₂ electrosynthesis (Supplementary Fig. 18), and catalyst leaching studies confirm that NiSe₂'s stability is maintained in the presence of dilute H₂O₂ oxidant (Supplementary Table 2). These experiments suggest that the unavoidable electroreduction of H₂O₂ could limit the maximum accumulated concentration of H₂O₂ and the overall selectivity practically achievable using these earth-abundant electrocatalysts, however, the electro-Fenton process of converting H₂O₂ to ·OH may allow us to utilize the produced H₂O₂ as an oxidant more efficiently by circumventing the undesired H₂O₂ electroreduction to water.

Glycerol valorization via the electro-Fenton process

To enable glycerol valorization by the electro-Fenton process, we operated NiSe₂/CFP cathode at the fixed potential of 0.60 V vs. RHE in O₂-saturated 0.1 M NaHSO₄/Na₂SO₄ buffer (pH ~ 2.8) containing Fe²⁺ and glycerol. The balanced equation shows that cathodic glycerol conversion consumes protons (Fig. 4a). To maintain the proton balance and stabilize the acidic pH in the cathodic half-cell, it is critical to place 0.05 M H₂SO₄ in the anode compartment to transport protons through the Nafion membrane (Supplementary Fig. 19). We used proton and carbon-13 nuclear magnetic resonance (¹H and ¹³C NMR) to identify and quantify the many

possible C₃, C₂, and C₁ products that can be sequentially formed from the oxidation of glycerol (Fig. 4b, details of NMR in Supplementary Fig. 20 and 21). Control experiments show that the electrogenerated H₂O₂ itself is not capable of oxidizing glycerol without the presence of Fe²⁺ (Supplementary Fig. 22), which confirms that the electro-Fenton process is indeed responsible for glycerol valorization at the cathode.

We further studied the impact of Fe²⁺ concentration ([Fe²⁺]) on the glycerol valorization via the electro-Fenton process. The rate of ·OH formation from the Fenton reaction should increase with higher [Fe²⁺] based on the rate law, but too much Fe²⁺ would consume the formed ·OH and decrease the oxidizing power (Fe²⁺ + ·OH + H⁺ → Fe³⁺ + H₂O)²⁹. After a controlled amount of charge is passed through NiSe₂/CFP cathode at 0.60 V vs. RHE (Supplementary Fig. 23), high glycerol conversion is achieved when [Fe²⁺] is 0.5 mM or 1.0 mM, while too little Fe²⁺ (0.1 mM) results in low glycerol conversion likely due to the slow ·OH formation (Fig. 4c). On the other hand, the selectivity toward all detected C₃ products [glyceraldehyde (GLAD), dihydroxyacetone (DHA), glyceric acid (GLA)] remain relatively high when [Fe²⁺] is 1.0 mM or below but decreases substantially when [Fe²⁺] is increased to 2.5 mM (Fig. 4c). One possible explanation is that at high [Fe²⁺], the high ·OH formation rate increases the relative concentration of ·OH to glycerol locally near the cathode, which might not be effectively dissipated even under vigorous stirring, driving the glycerol oxidation further to primarily C₂ [glycolaldehyde (GAD), glycolic acid (GA), glyoxylic acid (GLOA)] and C₁ [formic acid (FA)] products (Supplementary Fig. 24). This could also explain the relatively low glycerol conversion when [Fe²⁺] is 2.5 mM despite the fast ·OH formation rate (Fig. 4c). Overall, we identified 0.5 mM as the optimum [Fe²⁺] to concurrently achieve high glycerol conversion of up to ~55% and high C₃ product selectivity for cathodic valorization of glycerol (Fig. 4d and

Supplementary Table 3). As more charge is passed, the glycerol conversion steadily increases but the C₃ product selectivity decreases slightly due to the sequential oxidation of intermediate products. The gradual loss in the carbon balance of all detected aqueous phase organic products likely results from the eventual oxidation of FA to gaseous CO₂ undetectable by NMR (vide infra). The spent NiSe₂/CFP cathode was shown to be structurally and compositionally stable after the electro-Fenton process (Supplementary Fig. 25). These observations suggest that achieving an efficient electro-Fenton production of ·OH but maintaining a moderate concentration of this strongly oxidizing radical is the key to achieving high C₃ product selectivity and conversion from glycerol.

Linear paired glycerol valorization

To valorize glycerol at both cathode and anode concurrently, anodic glycerol oxidation needs to operate in acidic solution to match the pH requirement of the electro-Fenton process. Therefore, anodic glycerol oxidation was performed in an Ar-saturated H₂SO₄ solution containing 50 mM glycerol on an anode made by drop-casting commercial Pt/C catalyst^{12,13} on carbon fiber paper (Fig. 5a). This paired system needs to operate in a two-compartment H-cell (Fig. 5a) rather than in an undivided cell because the O₂ needed for the electro-Fenton process can undergo undesirable ORR on the Pt/C anode³⁹. Protons are transported through Nafion membrane and stabilize the pH of the catholyte (O₂-saturated NaHSO₄/Na₂SO₄ buffer containing 50 mM glycerol and 0.5 mM Fe²⁺, pH ~2.8) where the electro-Fenton process takes place.

Anodic glycerol oxidation at Pt/C anode in 0.05 M H₂SO₄ was first evaluated in the half-cell (Supplementary Fig. 26). To mimic the operation of the paired system, we applied a constant current of 1.7 mA (Supplementary Fig. 26c) to approximately match with the current on NiSe₂/CFP cathode in the electro-Fenton half-cell studies (Supplementary Fig. 23a). After a

controlled amount of charge was passed, the applied potential of Pt/C anode was relatively stable around 0.55 V vs. RHE, and glycerol was selectively oxidized into C₃ products [GLAD, DHA, GLA, hydroxypyruvic acid (HPA)] with very small quantities of C₂ (GA) and C₁ (FA) products (Supplementary Fig. 26e and Supplementary Table 3). The anodic half-cell studies show the viability of valorizing glycerol in a linear paired electrochemical system that theoretically could operate at a negligible external bias (< 0.05 V) with little external energy input needed if the internal resistance is negligible (Supplementary Note 1, also see the thermodynamic basis of this linear paired electrochemical system in Supplementary Note 2).

We then demonstrated the proof-of-concept linear paired electrochemical valorization of glycerol by feeding glycerol in both cathode and anode compartments of the H-cell where NiSe₂/CFP cathode was operated at 0.60 V vs. RHE and Pt/C anode matched the current (Supplementary Fig. 27 and 28). With 0.1 M NaHSO₄/Na₂SO₄ catholyte and 0.05 M H₂SO₄ anolyte, the paired system operated steadily at an external bias around 1 V (Fig. 5b, Condition I), and the product distributions in the catholyte and anolyte (Fig. 5c, Condition I) closely resembled those found in the respective half-cell studies under similar conditions, i.e., high percentage of C₃ products (*vide supra*). This external bias is higher than the theoretical value because there is a large solution IR drop between the anode and the reference electrode located on opposite sides of the membrane (Supplementary Fig. 28a and Supplementary Note 3).

When a higher supporting electrolyte concentration of 0.5 M was applied for both catholyte and anolyte, the paired system operated at a much lower external bias below 0.2 V (Fig. 5b, Condition II) due to the greatly reduced solution IR drop at the anode (Supplementary Fig. 28b). After a controlled amount of charge was passed, the product distributions in the anolyte were mostly unaffected (Fig. 5c, Condition II), whereas the detected aqueous phase organic

products in the catholyte slightly decreased (see possible explanations in Supplementary Note 4). The C₃ product selectivity in both catholyte and anolyte of the paired system decreased with increasing glycerol conversion up to ~53% (Fig. 5c and Supplementary Table 4), due to the sequential oxidation of intermediate products, similar to the respective half-cell studies (*vide supra*). Since FA was detected as a late-stage oxidation product in both catholyte and anolyte (Supplementary Table 4), control experiments suggested that both the electro-Fenton process and the anodic oxidation could further oxidize FA into gaseous CO₂ (Supplementary Fig. 29), which may account for the loss in the carbon balance of all detected aqueous products in both catholyte and anolyte (Supplementary Note 5). Finally, we note that the residual excess external bias of 0.2 V for this paired system appears to be mostly caused by the internal resistance, and the overall paired process can be viewed as a controlled partial oxidation of glycerol by oxygen gas, which should be thermodynamically spontaneous (see Supplementary Note 2). By employing zero-gap cell designs involving membrane electrode assemblies to lower the ohmic overpotential and by designing more active cathode and anode electrocatalysts to lower the kinetic overpotentials further, we believe that paired electrochemical systems for efficient glycerol valorization that need no external bias and no external energy input could be realized.

CONCLUSIONS

In summary, we demonstrated a linear paired electrochemical process for concurrent glycerol valorization by the electro-Fenton process at a stable and earth-abundant NiSe₂ cathode together with direct oxidation at a Pt anode. This process is enabled by the development of NiSe₂ as a highly selective and stable 2e⁻ ORR catalyst for H₂O₂ production in acidic solution, which is elucidated by calculated free energy diagrams and surface adsorbate analyses and experimentally

shown with RRDE and catalyst leaching studies together with sustained electrosynthesis of H_2O_2 . The electro-Fenton process at NiSe_2 cathode at the optimum operation conditions leads to efficient cathodic glycerol valorization with a high selectivity toward valuable C_3 oxidation products and high glycerol conversion of 55%. The linear paired system achieves similarly high glycerol conversion and product selectivity and can operate at a very small external bias below 0.2 V, which could theoretically be made into an unbiased system after further optimization in the future. The design principles for stable and selective electrocatalysts for acidic H_2O_2 production and the electro-Fenton process, and the conceptual strategy of linear pairing the electro-Fenton process with anodic oxidation presented here can open up new opportunities for electrochemical valorization of a variety of biomass feedstocks with high atom efficiency and low energy cost.

METHODS

Computational method

Spin polarized electronic structure calculations were performed using the Vienna Ab initio Simulation package (VASP)⁴⁰⁻⁴³ interfaced with the Atomic Simulation Environment (ASE)⁴⁴. Projector augmented wave (PAW) pseudopotentials^{45,46} with a cutoff of 450 eV were used to treat core electrons, and the Perdew–Burke–Ernzerhof (PBE) functional^{47,48} was used to treat exchange and correlation. Dispersion was treated using Grimme’s D3(ABC) method⁴⁹. To better describe the Co 3d electrons in *c*-CoSe₂, a Hubbard *U* parameter⁵⁰, *U*_{eff}= 2.0 eV, was taken from a previous report⁵¹. A variety of Hubbard *U* parameters were tested for *c*-NiSe₂, and were found to have little to no effect on the geometries or energies; therefore, no Hubbard *U* parameter was used for this catalyst. Solvation effects were treated using the continuum solvent method VASPsol^{52,53}. The Brillouin zone was sampled using a (10, 10, 10) and (10, 10, 1) Γ -centered Monkhorst–Pack mesh⁵⁴ for bulk and surface calculations, respectively. Lattice constants were determined by fitting to an equation of state (EOS)⁵⁵.

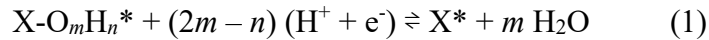
For both *c*-NiSe₂ and *c*-CoSe₂, their respective (100) surface exhibits the lowest surface energy compared to other crystal surfaces, and thus is the most thermodynamically stable surface [0.044 vs. 0.064 vs. 0.069 eV Å⁻² for *c*-CoSe₂ (100) vs. (110) vs. (111) surface³⁵; 0.036 vs. 0.053 vs. 0.058 eV Å⁻² for *c*-NiSe₂ (100) vs. (110) vs. (111) surface]. The (100) surfaces of *c*-NiSe₂ and *c*-CoSe₂ were modelled as a 1 × 1 unit cell slab with two repeats in the z-direction, leading to a total of 8 metal atoms and 16 Se atoms and a vacuum gap of at least 15 Å. The top half of the slabs was allowed to relax while the bottom half was frozen to simulate the bulk. For each ionic configuration, the electronic energy was converged below 10⁻⁶ eV. Both the clean slab and adsorbates were allowed to relax until the forces were converged below 0.005 eV Å⁻². Transition

states were located using the nudged elastic band (NEB) method^{56,57} and were refined using the dimer method⁵⁸⁻⁶⁰. All transition states were confirmed saddle points with one imaginary frequency corresponding to bond breaking. The atomic coordinates of the optimized computational models are provided in Supplementary Data 1.

Binding energies were calculated with respect to $O_{2(g)}$ and $H^{+}_{(aq)}$ and e^- . The energy of $H^{+}_{(aq)}$ and e^- was calculated using the computational hydrogen electrode (CHE) method⁶¹, where $H^{+}_{(aq)}$ is assumed to be in thermodynamic equilibrium with $H_{2(g)}$. The use of the CHE method for our calculation is validated by the fact that the difference in the OOH^* binding energy on the *c*-NiSe₂ (100) surface calculated by the CHE method vs. the grand-canonical density functional theory (GC-DFT) method, accounting for the change in surface charge density upon adsorption⁶²⁻⁶⁵, is < 0.1 eV and can be safely neglected. In order to avoid well-known errors in the DFT treatment of $O_{2(g)}$, the free energy of $O_{2(g)}$ was determined by matching the experimental standard equilibrium potential (1.229 V) of the reaction $1/2 O_{2(g)} + 2 H^{+}_{(aq)} + 2 e^- \rightarrow H_2O_{(l)}$. The adsorption of O_2 , forming O_2^* from $O_{2(g)}$, is excluded from our calculation because DFT does not treat $O_{2(g)}$ accurately, and the estimated free energy difference between $O_{2(g)}$ and O_2^* on the *c*-NiSe₂ (100) surface is < 0.1 eV and can be safely neglected. The free energies of species were calculated using $G = H - T \cdot S$, where H is the enthalpy including zero-point energy (ZPE) and thermal corrections, and S is either the total experimental entropy at 298 K and 1 bar (for gas phase species) or calculated under the harmonic approximation taking into account both vibrational contributions and hindered translations/rotations (for surface bound species). The free energy of $H_2O_{(l)}$ was calculated using the experimental free energy of formation for $H_2O_{(l)}$ and $H_2O_{(g)}$. The solvation free energy of $H_2O_{(aq)}$ was calculated using the experimental Henry's law constant⁶⁶. The calculated standard equilibrium potential (U_{RHE}^0) of the $2e^-$ ORR reaction $O_{2(g)} + 2 H^{+}_{(aq)} + 2$

$e^- \rightarrow H_2O_{(aq)}$ is 0.81 V, slightly higher than the experimental standard equilibrium potential of 0.69 V.

Free energies of different surface adsorbate coverages were calculated to predict the most thermodynamically stable surface termination of each catalyst for a given set of potential and pH conditions under the assumption that the surfaces can be approximated in equilibrium with $H_2O_{(l)}$.^{67,68} The equilibrated proton-coupled electron transfer reaction for a general surface intermediate can then be written as:



where X is the surface binding site, m is the number of oxygen atoms, and n is the number of hydrogen atoms. The free energy of this reaction can be written as:

$$\Delta G(U, pH) = G_{X^*} + m G_{H_2O} - G_{X-O_mH_n^*} - (2m - n) (G_{e^-} + G_{H^+}) \quad (2)$$

Using the computational hydrogen electrode (CHE) method^{61,69-71} ($G_{e^-} + G_{H^+} = \frac{1}{2}G_{H_2} - U_{SHE} - 2.303k_B \cdot T \cdot pH$) and converting the standard hydrogen electrode (SHE) to the reversible hydrogen electrode (RHE) ($U_{RHE} = U_{SHE} + 2.303k_B \cdot T \cdot pH$), the free energy can be rewritten as a function of U_{RHE} :

$$\Delta G(U_{RHE}) = G_{X^*} + m G_{H_2O} - G_{X-O_mH_n^*} - (2m - n) (\frac{1}{2}G_{H_2} - U_{RHE}) \quad (3)$$

A 1×1 unit cell slab of the (100) surface of each catalyst that has two metal binding sites and four Se binding sites was used to model intermediate surface coverages as a function of potential. For $c\text{-NiSe}_2$, the Ni site is the preferential binding site for both OH^* and O^* . For $c\text{-CoSe}_2$, the Co site is the preferential binding site for OH^* , and the Se site is the preferential binding site for O^* . A wide variety of surface coverages were examined on various combinations of binding sites. For the sake of clarity, only the most thermodynamically stable surface coverages (in the U_{RHE}

range of 0 V to 0.95 V) on the most preferential combination of binding sites were shown in Fig. 2c.

Chemicals

All chemicals were purchased from Sigma-Aldrich and used as received without further purification, unless noted otherwise. Deionized nanopure water (18.2 MΩ·cm) from Thermo Scientific Barnstead water purification systems was used for all experiments.

Materials synthesis

c-NiSe₂ powder sample was prepared by a hydrothermal method. Following a procedure modified from a previous report⁷², nickel hydroxide [Ni(OH)₂] precursor was first synthesized by dissolving 451.3 mg of NiSO₄·6H₂O (Acros Organics, 98+%) in 58.3 mL of water and 8.75 mL of 2 M ammonia aqueous solution (diluted from ammonium hydroxide solution, 28.0-30.0% NH₃ basis), and heating the solution at 180 °C for 24 h in a sealed 100-mL Teflon-lined stainless-steel autoclave. The resulting Ni(OH)₂ precursor was hydrothermally converted into *c*-NiSe₂ as follows: 4.29 g of NaOH (≥97.0%) and 571 mg of Se powder (≥99.5%) were suspended in 50 mL of water via sonication and heated at 220 °C for 24 h in a sealed 80-mL autoclave; upon cooling to room temperature, 35 mg of Ni(OH)₂ precursor was suspended in 10 mL of water and added dropwise into the Se-containing solution under vigorous stirring, and then heated at 180 °C for another 24 h in the same autoclave. The as-converted *c*-NiSe₂ product was successively washed with water, 1.25 M aqueous solution of Na₂S (nonahydrate, ≥98.0%) (to dissolve the elemental Se impurity⁷³), and water four times for each washing step, and dried under vacuum at 50 °C.

To prepare Ni(OH)₂ precursor on carbon fiber paper (Ni(OH)₂/CFP), Teflon-coated carbon fiber paper (Fuel Cell Earth, TGP-H-060) was first treated with oxygen plasma at 150 W power for 5

min for each side and annealed in air at 700 °C for 5 min. A 3 cm × 6 cm piece of annealed CFP was placed in the solution made of 2.1 mmol of $\text{Ni}(\text{NO}_3)_2 \cdot 6\text{H}_2\text{O}$ ($\geq 97.0\%$), 4.2 mmol of NH_4F ($\geq 98.0\%$), and 10.5 mmol of urea (99.0-100.5%) in 80 mL of water, and heated at 110 °C for 5 h in a sealed 100-mL autoclave. NiSe_2 /CFP was prepared by the same hydrothermal selenization method described above, except for using a 1.5 cm × 6 cm piece of $\text{Ni}(\text{OH})_2$ /CFP as the precursor. The as-converted NiSe_2 /CFP was immersed in 1.25 M aqueous solution of Na_2S three times to remove any excess elemental Se, rinsed with water and ethanol, and dried under N_2 gas flow. The areal loading of *c*- NiSe_2 grown on CFP was determined by the mass change of CFP after the materials growth. The *c*- CoSe_2 samples were prepared following the published procedures³⁵. All catalyst samples were stored in an argon-filled glove box to minimize the exposure to air.

Materials characterization

Powder X-ray diffraction (PXRD) patterns were collected on a Bruker D8 ADVANCE powder X-ray diffractometer using $\text{Cu K}\alpha$ radiation. Scanning electron microscopy (SEM) was performed on a Zeiss SUPRA 55VP field emission scanning electron microscope at an accelerating voltage of 1 kV. For SEM imaging, powder samples were drop-casted onto silicon wafer substrates. X-ray photoelectron spectroscopy (XPS) was performed on a Thermo Scientific K-Alpha XPS system with an $\text{Al K}\alpha$ X-ray source. Raman spectroscopy was performed on a Thermo Fisher Scientific DXR3xi Raman Imaging Microscope using a 50 μm confocal pinhole aperture and a 532 nm laser source and with a low laser power of 0.1 mW and an exposure time of 1.0 second to avoid sample degradation. For XPS and Raman experiments, powder samples were drop-casted onto graphite substrates, which were made by cutting thin slices of graphite rod (Graphite Store, low wear EDM rod), abrading with 600 grit silicon carbide paper (Allied High

Tech Products), and sonicating in water and ethanol until clean. X-ray absorption spectroscopy (XAS) of NiSe₂/CFP before and after electrochemical testing was performed in transmission mode at the Advanced Photon Source (APS) Beamline 10-BM-B, and analyzed using ATHENA and ARTEMIS software⁷⁴.

Electrode preparation

Drop-casted catalysts were prepared on a rotating ring-disk electrode (RRDE-3A, ALS Co., Ltd) made of a glassy carbon disk (with a geometric area of 0.126 cm²_{disk}) surrounded by a Pt ring. The collection efficiency of the bare RRDE was 0.43, determined experimentally using the ferri-/ferrocyanide redox couple. The RRDE was successively polished with 1, 0.3, and 0.05 µm alumina suspensions (Allied High Tech Products) on a polishing cloth (Buehler, MicroCloth), thoroughly rinsed with water and methanol, briefly sonicated in methanol for < 20 s, and dried under ambient conditions before use. The catalyst inks were prepared by suspending pre-weighed catalyst powders in desired volumes of a 9 : 1 (v/v) mixture of water and 5 wt% Nafion solution by sonication for 1 h. A fixed volume (10 µL) of catalyst ink was then drop-casted on the disk electrode and dried under ambient conditions at a rotation rate of 700 rpm to form a uniform catalyst film where the Nafion loading was identical (0.4 mg_{Nafion} cm⁻²_{disk}) whereas the catalyst loading was varied (Fig. 3a and 3b). NiSe₂/CFP cathode was fabricated from as-synthesized NiSe₂/CFP sample (vide supra) by using 5-min epoxy (Devcon) to define the exposed geometric area as ~1 cm × ~1 cm. The Pt/C anode was prepared by drop-casting 200 µL of the catalyst ink (50 mg of 20 wt% Pt/C suspended in 900 µL of isopropanol and 100 µL of 5 wt% Nafion solution by sonication for 1.5 h) on both sides (100 µL on each side) of the pre-fabricated bare CFP electrode (~1 cm × ~1 cm), resulting in a catalyst loading of ~2 mg_{Pt} cm⁻²_{geo}.

Rotating ring-disk electrode measurement

RRDE measurements were conducted in an undivided three-electrode cell with a graphite rod counter electrode and a Hg/Hg₂SO₄ (saturated K₂SO₄) reference electrode (calibrated against a saturated calomel electrode) connected to a Bio-Logic VMP-300 multichannel potentiostat. All potentials were reported versus RHE (E vs. RHE = E vs. SHE + 0.059 × pH). Prior to RRDE measurements, the electrolyte solution (40–45 mL) of either 0.05 M H₂SO₄ (pH ~1.2) or 0.1 M NaHSO₄/Na₂SO₄ buffer solution (pH~2.8) was purged with O₂ gas for >10 min, and a blanket of O₂ gas was maintained above the electrolyte solution during the measurements. Under O₂-saturated condition, the catalyst-coated disk was first conditioned by running cyclic voltammetry (CV) between -0.025 V and 0.75 V vs. RHE at 100 mV s⁻¹ and 1600 rpm for 10 cycles, while holding the Pt ring at 1.3 V vs. RHE. The Pt ring was then conditioned by running CV between 0.05 V and 1.20 V vs. RHE at 100 mV s⁻¹ and 1600 rpm for 10 cycles while holding the disk at 0.75 V vs. RHE to remove the surface PtO_x^{75,76}. The 2e⁻ ORR catalytic properties were evaluated by performing linear sweep voltammetry of the catalyst-coated disk from 0.75 to -0.025 V vs. RHE at 50 mV s⁻¹ and various rotation rates, meanwhile holding the Pt ring at 1.3 V vs. RHE. Finally, the background current, double-layer capacitance (C_{dl} , determined by CV of the disk between -0.025 V and 0.75 V vs. RHE at various scan rates and 0 rpm), and uncompensated resistance (R_u , determined by electrochemical impedance spectroscopy of the disk at 0.75 V vs. RHE) were measured under Ar-saturated conditions. By manually conducting background current and iR corrections, the H₂O₂ selectivity (p_{RRDE}) is calculated as follows:

$$p_{RRDE} (\%) = \frac{2 \times \frac{i_{ring}}{N}}{i_{disk} + \frac{i_{ring}}{N}} \times 100\% \quad (4)$$

where i_{disk} and i_{ring} are the respective disk and ring current, and N is the collection efficiency. For the ease of visualizing the H₂O₂ selectivity from RRDE voltammograms (Fig. 3a), both disk and

ring current densities (j_{disk} and j_{ring}) are normalized to the geometric area of the disk electrode (A_{disk}), and the ring current density is further adjusted by the collection efficiency:

$$j_{\text{disk}} = \frac{i_{\text{disk}}}{A_{\text{disk}}} \quad (5)$$

$$j_{\text{ring}} = \frac{i_{\text{ring}}}{A_{\text{disk}} \times N} = j_{\text{peroxide}} \quad (6)$$

where j_{peroxide} is the partial current density for H_2O_2 production.

The protocols for long-term RRDE stability tests were described in Supplementary Fig 7. After these stability tests, the spent catalysts were recovered from the disk electrode by sonicating in water and ultracentrifuging at 13200 rpm for 1 min, followed by re-dispersing in minimal amount of water and drop-casting onto graphite substrates for XPS and Raman characterization (vide supra). To monitor the catalyst leaching during these stability tests, the spent electrolyte solutions were filtered with 0.22- μm syringe filters (Restek) and then analyzed with inductively coupled plasma mass spectrometry (ICP-MS) measurements on an Agilent 8900 Triple Quadrupole ICP-MS spectrometer. ICP-MS standard solutions were prepared by dissolving $\text{NiSO}_4 \cdot 6\text{H}_2\text{O}$ ($\geq 98\%$), or $\text{CoSO}_4 \cdot 7\text{H}_2\text{O}$ ($\geq 99\%$), or SeO_2 ($\geq 99.9\%$) in a matrix solution of 0.05 M H_2SO_4 ($\text{pH} \sim 1.2$) or 0.1 M $\text{NaHSO}_4/\text{Na}_2\text{SO}_4$ ($\text{pH} \sim 2.8$).

Bulk electrosynthesis of H_2O_2

NiSe_2/CFP cathode (vide supra) was used for constant-potential bulk electrosynthesis of H_2O_2 in O_2 -saturated 0.05 M H_2SO_4 ($\text{pH} \sim 1.2$) or 0.1 M $\text{NaHSO}_4/\text{Na}_2\text{SO}_4$ ($\text{pH} \sim 2.8$) solution (4 mL, stirred at 1200 rpm) placed in the cathode compartment of a two-compartment three-electrode H-cell (see Supplementary Fig. 12). Nafion 117 membrane (Fuel Cell Store) was cleaned by successively immersing in 3 wt% H_2O_2 , water, 1 M H_2SO_4 , and water at 80 °C for 1 h for each cleaning step, and stored in 0.05 M H_2SO_4 at room temperature before use. NiSe_2/CFP cathode

was conditioned by running CV between -0.025 V and 0.75 V vs. RHE at 100 mV s⁻¹ for 5 cycles to reach the steady state before use. Chronoamperometry was then performed to produce H₂O₂ at NiSe₂/CFP cathode, and the optimum operating potential was found to be 0.60 V vs. RHE (see Fig. 3d). A small aliquot (25 µL) of catholyte was periodically sampled during chronoamperometry and mixed with 8 mL of Ce(SO₄)₂ stock solution (~0.4 mM Ce⁴⁺ in 0.5 M H₂SO₄ matrix solution) to chemically detect the produced H₂O₂ by UV-Vis spectrophotometry at 318 nm (2 Ce⁴⁺ + H₂O₂ → 2 Ce³⁺ + O₂ + 2 H⁺). The concentration of the produced H₂O₂ can be calculated as follows:

$$[\text{H}_2\text{O}_2] = \frac{8 \text{ mL} \times [\text{Ce}^{4+}]_{\text{before}} - 8.025 \text{ mL} \times [\text{Ce}^{4+}]_{\text{after}}}{2 \times 0.025 \text{ mL}} \quad (7)$$

where [H₂O₂] is the cumulative H₂O₂ concentration, [Ce⁴⁺]_{before} and [Ce⁴⁺]_{after} are the [Ce⁴⁺] in the stock solution (determined by fitting to the standard curve) before and after mixing with the catholyte aliquot. The cumulative H₂O₂ yield (*n*_{H₂O₂}), H₂O₂ selectivity (*p*_{H₂O₂}), and Faradaic efficiency (FE_{H₂O₂}) are calculated based on [H₂O₂], the catholyte volume (taking into account the evaporation), and the total amount of charge passed (*Q*_{total}) (see detailed methodology for these calculations described in our previous report³⁵):

$$p_{\text{H}_2\text{O}_2} (\%) = \frac{n_{\text{H}_2\text{O}_2} (\text{mol})}{n_{\text{H}_2\text{O}_2} (\text{mol}) + \frac{Q_{\text{total}} (\text{C}) - 2 \times n_{\text{H}_2\text{O}_2} (\text{mol}) \times F}{4 \times F}} \times 100\% \quad (8)$$

$$\text{FE}_{\text{H}_2\text{O}_2} (\%) = \frac{2 \times n_{\text{H}_2\text{O}_2} (\text{mol}) \times F}{Q_{\text{total}} (\text{C})} \times 100\% \quad (9)$$

where *F* is the Faraday constant (96485 C mol⁻¹). To monitor the catalyst leaching during H₂O₂ bulk electrosynthesis, the spent catholytes were filtered with 0.22-µm syringe filters (Restek) and diluted by 15 times with a matrix solution of 0.05 M H₂SO₄ for ICP-MS analysis (vide supra).

Glycerol valorization and product analysis

All experiments of glycerol valorization were performed in the two-compartment three-electrode H-cell described above. Half-cell studies of glycerol valorization via the electro-Fenton process at NiSe₂ cathode were performed by chronoamperometry with controlled amounts of charge passed at 0.60 V vs. RHE in O₂-saturated 0.1 M NaHSO₄/Na₂SO₄ solution (pH ~2.8) containing glycerol (~50 mM) and Fe²⁺ (0.1, 0.5, 1.0, or 2.5 mM, prepared from FeSO₄·7H₂O, ≥99.0%) (see schematic in Supplementary Fig. 19). Half-cell studies of direct oxidation of glycerol at Pt/C anode were performed by chronopotentiometry with controlled amounts of charge passed at 1.7 mA in Ar-saturated 0.05 M H₂SO₄ solution (pH ~1.2) containing glycerol (~50 mM) (see schematic in Supplementary Fig. 26). Linear paired glycerol valorization at the NiSe₂ cathode (in O₂-saturated 0.1 M or 0.5 M NaHSO₄/Na₂SO₄ solution containing ~50 mM glycerol and 0.5 mM Fe²⁺, pH ~2.8) and Pt/C anode (in Ar-saturated H₂SO₄ solution containing ~50 mM glycerol) was performed by operating the cathode via chronoamperometry at 0.60 V vs. RHE while recording the applied potential of the anode (see schematic in Supplementary Fig. 27). The analysis of the products from glycerol valorization was performed by ¹H and ¹³C NMR spectroscopy on a Bruker AVANCE III 600 MHz NMR spectrometer. Glycerol (≥99.0%), DL-glyceraldehyde (≥90%), dihydroxyacetone (Pharmaceutical Secondary Standard; Certified Reference Material), DL-glyceric acid (TCI America, 20% in water, ca. 2 mol/L), β-hydroxypyruvic acid (≥95.0%), tartronic acid (Alfa Aesar, 98%), sodium mesoxalate monohydrate (≥98.0%), glycolaldehyde dimer (crystalline, mixture of stereoisomers), glycolic acid (99%), glyoxylic acid monohydrate (98%), oxalic acid (99.999%), and formic acid (≥98%) were individually prepared into NMR standard samples (500 μL) in Norell® Sample Vault Series™ NMR tubes (diam. × L 5 mm × 178 mm) using D₂O (99.9 atom % D) as the solvent and maleic acid (Standard for quantitative NMR, TraceCERT®) as the internal standard¹⁵ (detailed

ratios among the different components in these NMR samples are described in Supplementary Fig. 20 and 21). To achieve quantitative ^1H NMR results, the relaxation delay was set to 20 seconds (longer than 5 times of the T1 relaxation times of all compounds of interest determined by inversion recovery experiments), and the zgcppr.UW pulse sequence was used for the solvent suppression, and 4 scans were collected. For ^{13}C NMR results, the relaxation delay was set to 2 seconds, and 256 scans were collected. After the half-cell or linear paired glycerol valorization experiments, the catholytes and/or anolytes of interest were filtered with 0.22- μm syringe filters (Restek) and prepared into NMR samples accordingly (detailed ratios among the different components in these NMR samples are described in Supplementary Fig. 22, 23, 24). The quantifications of $[\text{glycerol}]_i$, $[\text{glycerol}]_f$, and $[\text{C}_n \text{ product}]_f$ are based on the selected ^1H NMR peak integration ratios relative to the maleic acid internal standard (see peak assignments and peak selections in Supplementary Fig. 20). The glycerol conversion, C_n product selectivity ($n = 1, 2, 3$), and carbon balance of all detected aqueous phase organic products are calculated as follows:

$$\text{glycerol conversion (\%)} = \frac{[\text{glycerol}]_i \times V_i - [\text{glycerol}]_f \times V_f}{[\text{glycerol}]_i \times V_i} \times 100\% \quad (10)$$

$$\text{C}_n \text{ product selectivity (\%)} = \frac{\frac{n}{3} \times [\text{C}_n \text{ product}]_f \times V_f}{[\text{glycerol}]_i \times V_i - [\text{glycerol}]_f \times V_f} \times 100\% \quad (11)$$

$$\text{carbon balance (\%)} = \frac{3 \times [\text{glycerol}]_f \times V_f + \sum_{n=1}^3 \{n \times [\text{C}_n \text{ product}]_f \times V_f\}}{3 \times [\text{glycerol}]_i \times V_i} \times 100\% \quad (12)$$

where V_i and V_f are the initial and final electrolyte volume, $[\text{glycerol}]_i$ and $[\text{glycerol}]_f$ are the initial and final concentration of glycerol, $[\text{C}_n \text{ product}]_f$ is the final concentration of C_n product ($n = 1, 2, 3$), all of which are listed in Supplementary Table 3 and 4. The Faradaic efficiency of all detected aqueous phase organic products at the anode (FE_{anode}) and the cathode ($\text{FE}_{\text{cathode}}$) are

calculated and estimated, respectively, based on the methods described in Supplementary Note 6, and these calculated FE_{anode} and estimated $FE_{cathode}$ values are also listed in Supplementary Table 3 and 4.

DATA AVAILABILITY

The data that support the findings of this study are presented in the article and the Supplementary Information. Any other relevant data are also available from the corresponding authors upon reasonable request. Source data are provided with this paper.

ACKNOWLEDGEMENTS

This research was supported by the National Science Foundation (NSF) Grant CHE-1955074 for the materials synthesis and the electrochemical experiments (H.S., R.D.R., and S.J.) and for the computational modelling (A.N.J., K.L., and J.R.S.). The calculations here utilized the computational resources from the Extreme Science and Engineering Discovery Environment (XSEDE) supported by NSF Grant TG-CHE120088. The Bruker AVANCE III 600 MHz NMR spectrometer was supported by the National Institutes of Health (NIH) grant S10 OK012245. The authors gratefully acknowledge use of facilities and instrumentation at the UW-Madison Wisconsin Centers for Nanoscale Technology (wcnt.wisc.edu) partially supported by the NSF through the University of Wisconsin Materials Research Science and Engineering Center (DMR-1720415). We thank Mr. James Lazarcik for his help with gaining access to the ICP-MS spectrometer supported by the Water Science and Engineering Laboratory (WSEL) at UW-Madison. This research used resources of the Advanced Photon Source (APS), a U.S. Department of Energy (DOE) Office of Science User Facility operated for the DOE Office of

Science by Argonne National Laboratory under Contract No. DE-AC02-06CH11357, and we thank Dr. Yujia Ding for her help with the XAS experiments performed at the APS Beamline 10-BM-B.

AUTHOR CONTRIBUTIONS

H.S. and S.J. designed the experiments. H.S. carried out the materials synthesis, materials characterization with the help of R.D.R., the electrochemical measurements, and the product analyses of glycerol valorization with the help of H.H. A.N.J. and J.R.S. conceived the computational modelling of the catalyst. A.N.J. and K.L. performed the computational modelling. H.S. and S.J. wrote the manuscript, and all authors commented on the manuscript.

COMPETING INTERESTS

A provisional patent has been filed based on this work by some of the authors of this manuscript (H.S., A.N.J., R.D.R., K.L., J.R.S., S.J.). The remaining authors (H. H.) declare no competing interests.

FIGURE LEGENDS/CAPTIONS

Fig. 1. Different pairing strategies for electrochemical valorization of glycerol. (a) In previous work, anodic oxidation of glycerol is paired either with $4e^-$ ORR in a galvanic cell or with HER or CO_2 /CORR in an electrolytic cell. (b) In this work, cathodic valorization of glycerol enabled by the electro-Fenton process at a stable $NiSe_2$ cathode is further paired with anodic oxidation and integrated into a linear paired electrochemical process to concurrently produce the same glycerol-derived oxidation products at both cathode and anode.

Fig. 2. Computations of ORR energetics and surface stability of *c*-NiSe₂ vs. *c*-CoSe₂. (a) Crystal structures of *c*-NiSe₂ and *c*-CoSe₂. (b) Calculated free energy diagrams of the 2e⁻ vs. 4e⁻ ORR pathway on the *c*-NiSe₂ vs. *c*-CoSe₂ (100) surface at U_{RHE}^0 . The transition state for OOH* cleavage (OOH* + * → O* + OH*) is denoted as TS. (c) Different coverages of O* and/or OH* (top) and comparisons of their free energies (bottom) on the *c*-NiSe₂ vs. *c*-CoSe₂ (100) surface in equilibrium with water. The binding energies of O* and OH* on their preferential binding sites at U_{RHE}^0 are shown as the bottom insets in panel c. The yellow shaded regions indicate the potential range where the adsorbate-free clean surface is lower in free energy compared to the O*- and/or OH*-adsorbed surfaces. The inset images show the co-adsorption of one O* and one OH* to their preferential binding sites on the surface unit cell comprising of two metal sites and four Se sites. The Ni, Co, Se, O, and H atoms are displayed in green, magenta, orange, red, and white, respectively.

Fig. 3. Electrocatalytic properties and stability for acidic H₂O₂ electrosynthesis. (a) RRDE voltammograms recorded at 1600 rpm and (b) the H₂O₂ selectivity profiles of drop-casted *c*-NiSe₂ (left) and *c*-CoSe₂ (right) catalysts with various catalyst loadings in O₂-saturated 0.05 M H₂SO₄ (pH ~1.2). (c) Normalized metal and selenium leaching rates of drop-casted *c*-NiSe₂ and *c*-CoSe₂ catalysts during RRDE stability tests in O₂-saturated 0.05 M H₂SO₄ (pH ~1.2, left) and 0.1 M NaHSO₄/Na₂SO₄ buffer (pH ~2.8, right). For each catalyst, the error bars result from four RRDE stability tests at different catalyst loadings (Supplementary Table 1). (d) The cumulative H₂O₂ yield (left) and H₂O₂ selectivity (right) after 6 hours for four trials of H₂O₂ bulk electrosynthesis in O₂-saturated 0.05 M H₂SO₄ (4 mL, stirred at 1200 rpm) using four NiSe₂/CFP

electrodes ($\sim 1.06 \text{ mg}_{\text{Ni}} \text{ cm}^{-2}_{\text{geo}}$, $\sim 1 \text{ cm}^2_{\text{geo}}$) operated at different fixed applied potentials (0.50, 0.55, 0.60, 0.65 V vs. RHE) (see details in Supplementary Fig. 13). (e) Long-term (37 h) sustained bulk electrosynthesis of H_2O_2 in O_2 -saturated 0.05 M H_2SO_4 at the optimum potential of 0.60 V vs. RHE using one NiSe_2/CFP electrode repeatedly for five consecutive runs (see details in Supplementary Fig. 16).

Fig. 4. Glycerol valorization enabled by the electro-Fenton process at NiSe_2 cathode. (a) Balanced equation of cathodic glycerol valorization, which suggests proton consumption. (b) Possible reaction pathways of glycerol oxidation into various C_3 , C_2 , and C_1 products by the electro-Fenton process at NiSe_2/CFP cathode. The detected (or anticipated) and undetected products are labeled based on NMR analyses. (c) Glycerol conversion (left) and the selectivity toward all detected C_3 products (right) as a function of $[\text{Fe}^{2+}]$ (0.1, 0.5, 1.0, or 2.5 mM) after passing a controlled amount of charge through NiSe_2/CFP cathode in O_2 -saturated 0.1 M $\text{NaHSO}_4/\text{Na}_2\text{SO}_4$ buffer (pH ~ 2.8) starting with ~ 50 mM glycerol under vigorous stirring (see details in Supplementary Fig. 23 and 24). (c) Aqueous phase organic (C_3 , C_2 , and C_1) product selectivity, glycerol conversion percentage, and carbon balance of all detected aqueous phase organic products for cathodic valorization of glycerol (~ 50 mM) under the optimum $[\text{Fe}^{2+}]$ of 0.5 mM.

Fig. 5. Linear paired glycerol valorization at NiSe_2 cathode and Pt anode. (a) Schematic illustration and working principle of the linear paired system in a two-compartment H-cell (see details in Supplementary Fig. 27). (b) The cathode current and external bias over time, which shows the steady operation of the linear paired system comprising of a NiSe_2/CFP cathode

(~ 1.24 mg_{Ni} cm⁻²_{geo}, ~ 1 cm²_{geo}) operated at 0.60 V vs. RHE in O₂-saturated NaHSO₄/Na₂SO₄ buffer (pH ~ 2.8 , containing ~ 50 mM glycerol and 0.5 mM Fe²⁺) and a Pt/C anode (~ 2 mg_{Pt} cm⁻²_{geo}, ~ 1 cm²_{geo}) operated in Ar-saturated H₂SO₄ solution (containing ~ 50 mM glycerol). The current and bias are influenced by different supporting electrolyte concentrations (Condition I: 0.1 M NaHSO₄/Na₂SO₄ for catholyte, and 0.05 M H₂SO₄ for anolyte; Condition II: 0.5 M NaHSO₄/Na₂SO₄ for catholyte, and 0.5 M H₂SO₄ for anolyte). For both current and bias, average \pm standard deviation is calculated for each electrolysis run from all the collected data points (see Source Data). (c) Product selectivity, glycerol conversion percentage, and carbon balance of all detected aqueous phase organic (C₃, C₂, and C₁) products for linear paired electrochemical valorization of glycerol under different supporting electrolyte conditions (I and II, as described in panel b).

REFERENCES

1. Luna, P. D. et al. What would it take for renewably powered electrosynthesis to displace petrochemical processes? *Science* **364**, eaav3506 (2019).
2. Tang, C., Zheng, Y., Jaroniec, M. & Qiao, S.-Z. Electrocatalytic refinery for sustainable production of fuels and chemicals. *Angew. Chem. Int. Ed.* **60**, 19572-19590 (2021).
3. Lucas, F. W. S. et al. Electrochemical routes for the valorization of biomass-derived feedstocks: From chemistry to application. *ACS Energy Lett.* **6**, 1205-1270 (2021).
4. Werpy, T. & Petersen, G. Top value added chemicals from biomass: Volume I -- Results of screening for potential candidates from sugars and synthesis gas. (United States, 2004).
5. Da Silva Ruy, A. D., Ferreira, A. L. F., Bresciani, A. É., de Brito Alves, R. M. & Pontes, L. A. M. Market prospecting and assessment of the economic potential of glycerol from biodiesel. *Biotechnological Applications of Biomass*. IntechOpen, 2020.
6. Pagliaro, M., Ciriminna, R., Kimura, H., Rossi, M. & Della Pina, C. From glycerol to value-added products. *Angew. Chem. Int. Ed.* **46**, 4434-4440 (2007).
7. Katryniok, B. et al. Selective catalytic oxidation of glycerol: perspectives for high value chemicals. *Green Chem.* **13**, 1960-1979 (2011).
8. Dodekatos, G., Schünemann, S. & Tüysüz, H. Recent advances in thermo-, photo-, and electrocatalytic glycerol oxidation. *ACS Catal.* **8**, 6301-6333 (2018).
9. Simões, M., Baranton, S. & Coutanceau, C. Electrochemical valorisation of glycerol. *ChemSusChem* **5**, 2106-2124 (2012).

10. Li, T. & Harrington, D. A. An overview of glycerol electrooxidation mechanisms on Pt, Pd and Au. *ChemSusChem* **14**, 1472-1495 (2021).
11. Kwon, Y., Schouten, K. J. P. & Koper, M. T. M. Mechanism of the catalytic oxidation of glycerol on polycrystalline gold and platinum electrodes. *ChemCatChem* **3**, 1176-1185 (2011).
12. Kwon, Y., Birdja, Y., Spanos, I., Rodriguez, P. & Koper, M. T. M. Highly selective electro-oxidation of glycerol to dihydroxyacetone on platinum in the presence of bismuth. *ACS Catal.* **2**, 759-764 (2012).
13. Lee, S. et al. Highly selective transformation of glycerol to dihydroxyacetone without using oxidants by a PtSb/C-catalyzed electrooxidation process. *Green Chem.* **18**, 2877-2887 (2016).
14. Fan, L. et al. Recent progress in electrocatalytic glycerol oxidation. *Energy Technol.* **9**, 2000804 (2021).
15. Li, Y., Wei, X., Chen, L., Shi, J. & He, M. Nickel-molybdenum nitride nanoplate electrocatalysts for concurrent electrolytic hydrogen and formate productions. *Nat. Commun.* **10**, 5335 (2019).
16. Han, X. et al. Electrocatalytic oxidation of glycerol to formic acid by CuCo₂O₄ spinel oxide nanostructure catalysts. *ACS Catal.* **10**, 6741-6752 (2020).
17. Simões, M., Baranton, S. & Coutanceau, C. Electro-oxidation of glycerol at Pd based nano-catalysts for an application in alkaline fuel cells for chemicals and energy cogeneration. *Appl. Catal. B: Environ.* **93**, 354-362 (2010).
18. Chen, Y. X. et al. Nanotechnology makes biomass electrolysis more energy efficient than water electrolysis. *Nat. Commun.* **5**, 4036 (2014).
19. Dagdougui, H., Sacile, R., Bersani, C. & Ouammi, A. Chapter 2 - Hydrogen Production and Current Technologies. In: Dagdougui, H., Sacile, R., Bersani, C. & Ouammi, A. (eds). *Hydrogen Infrastructure for Energy Applications*. Academic Press, 2018, pp 7-21.
20. Liu, D. et al. Selective photoelectrochemical oxidation of glycerol to high value-added dihydroxyacetone. *Nat. Commun.* **10**, 1779 (2019).
21. Verma, S., Lu, S. & Kenis, P. J. A. Co-electrolysis of CO₂ and glycerol as a pathway to carbon chemicals with improved technoeconomics due to low electricity consumption. *Nat. Energy* **4**, 466-474 (2019).
22. Yadegari, H. et al. Glycerol oxidation pairs with carbon monoxide reduction for low-voltage generation of C₂ and C₃ product streams. *ACS Energy Lett.* **6**, 3538-3544 (2021).
23. Li, R., Xiang, K., Peng, Z., Zou, Y. & Wang, S. Recent advances on electrolysis for simultaneous generation of valuable chemicals at both anode and cathode. *Adv. Energy Mater.* **11**, 2102292 (2021).
24. Aust, N. & Kirste, A. Paired Electrosynthesis. In: Kreysa, G., Ota, K.-i. & Savinell, R. F. (eds). *Encyclopedia of Applied Electrochemistry*. Springer New York: New York, NY, 2014, pp 1505-1510.
25. Ibanez, J. G., Frontana-Uribe, B. A. & Vasquez-Medrano, R. Paired electrochemical processes: overview, systematization, selection criteria, design strategies, and projection. *J. Mex. Chem. Soc.* **60**, 247-260 (2016).
26. Strehl, J., Abraham, M. L. & Hilt, G. Linear paired electrolysis—Realising 200% current efficiency for stoichiometric transformations—The electrochemical bromination of alkenes. *Angew. Chem. Int. Ed.* **60**, 9996-10000 (2021).

27. Yang, S. et al. Toward the decentralized electrochemical production of H₂O₂: A focus on the catalysis. *ACS Catal.* **8**, 4064-4081 (2018).

28. Perry, S. C. et al. Electrochemical synthesis of hydrogen peroxide from water and oxygen. *Nat. Rev. Chem.* **3**, 442-458 (2019).

29. Brillas, E., Sirés, I. & Oturan, M. A. Electro-Fenton process and related electrochemical technologies based on Fenton's reaction chemistry. *Chem. Rev.* **109**, 6570-6631 (2009).

30. Teong, S. P., Li, X. & Zhang, Y. Hydrogen peroxide as an oxidant in biomass-to-chemical processes of industrial interest. *Green Chem.* **21**, 5753-5780 (2019).

31. Moody, G. J. The action of fenton's reagent on carbohydrates. *Tetrahedron* **19**, 1705-1710 (1963).

32. Vitale, A. A., Bernatene, E. A., Vitale, M. G. & Pomilio, A. B. New insights of the Fenton reaction using glycerol as the experimental model. Effect of O₂, inhibition by Mg²⁺, and oxidation state of Fe. *J. Phys. Chem. A* **120**, 5435-5445 (2016).

33. Zeng, J. et al. Biomimetic Fenton-catalyzed lignin depolymerization to high-value aromatics and dicarboxylic acids. *ChemSusChem* **8**, 861-871 (2015).

34. Sheng, H. et al. Electrocatalytic production of H₂O₂ by selective oxygen reduction using earth-abundant cobalt pyrite (CoS₂). *ACS Catal.* **9**, 8433-8442 (2019).

35. Sheng, H. et al. Stable and selective electrosynthesis of hydrogen peroxide and the electro-Fenton process on CoSe₂ polymorph catalysts. *Energy Environ. Sci.* **13**, 4189-4203 (2020).

36. Siahrostami, S. et al. Enabling direct H₂O₂ production through rational electrocatalyst design. *Nat. Mater.* **12**, 1137-1143 (2013).

37. Siahrostami, S. et al. A review on challenges and successes in atomic-scale design of catalysts for electrochemical synthesis of hydrogen peroxide. *ACS Catal.* **10**, 7495-7511 (2020).

38. The Materials Project. <https://materialsproject.org/> (Accessed December 2021).

39. Ryu, J. et al. Thermochemical aerobic oxidation catalysis in water can be analysed as two coupled electrochemical half-reactions. *Nat. Catal.* **4**, 742-752 (2021).

40. Kresse, G. & Hafner, J. Ab initio molecular dynamics for liquid metals. *Phys. Rev. B* **47**, 558-561 (1993).

41. Kresse, G. & Hafner, J. Ab initio molecular-dynamics simulation of the liquid-metal--amorphous-semiconductor transition in germanium. *Phys. Rev. B* **49**, 14251-14269 (1994).

42. Kresse, G. & Furthmüller, J. Efficiency of ab-initio total energy calculations for metals and semiconductors using a plane-wave basis set. *Comput. Mater. Sci.* **6**, 15-50 (1996).

43. Kresse, G. & Furthmüller, J. Efficient iterative schemes for ab initio total-energy calculations using a plane-wave basis set. *Phys. Rev. B* **54**, 11169-11186 (1996).

44. Bahn, S. R. & Jacobsen, K. W. An object-oriented scripting interface to a legacy electronic structure code. *Comput. Sci. Eng.* **4**, 56-66 (2002).

45. Blöchl, P. E. Projector augmented-wave method. *Phys. Rev. B* **50**, 17953-17979 (1994).

46. Kresse, G. & Joubert, D. From ultrasoft pseudopotentials to the projector augmented-wave method. *Phys. Rev. B* **59**, 1758-1775 (1999).

47. Perdew, J. P., Burke, K. & Ernzerhof, M. Generalized gradient approximation made simple. *Phys. Rev. Lett.* **77**, 3865-3868 (1996).

48. Perdew, J. P., Burke, K. & Ernzerhof, M. Generalized gradient approximation made simple [Phys. Rev. Lett. 77, 3865 (1996)]. *Phys. Rev. Lett.* **78**, 1396-1396 (1997).

49. Grimme, S., Antony, J., Ehrlich, S. & Krieg, H. A consistent and accurate ab initio parametrization of density functional dispersion correction (DFT-D) for the 94 elements H-Pu. *J. Chem. Phys.* **132**, 154104 (2010).

50. Anisimov, V. I., Zaanen, J. & Andersen, O. K. Band theory and Mott insulators: Hubbard U instead of Stoner *I. Phys. Rev. B* **44**, 943-954 (1991).

51. Wu, X. et al. Metal organic framework derived Fe-doped CoSe₂ incorporated in nitrogen-doped carbon hybrid for efficient hydrogen evolution. *ACS Sustain. Chem. Eng.* **6**, 8672-8678 (2018).

52. Mathew, K., Sundararaman, R., Letchworth-Weaver, K., Arias, T. A. & Hennig, R. G. Implicit solvation model for density-functional study of nanocrystal surfaces and reaction pathways. *J. Chem. Phys.* **140**, 084106 (2014).

53. Mathew, K., Kolluru, V. S. C., Mula, S., Steinmann, S. N. & Hennig, R. G. Implicit self-consistent electrolyte model in plane-wave density-functional theory. *arXiv*, 1601.03346 (2019).

54. Monkhorst, H. J. & Pack, J. D. Special points for Brillouin-zone integrations. *Phys. Rev. B* **13**, 5188-5192 (1976).

55. Alchagirov, A. B., Perdew, J. P., Boettger, J. C., Albers, R. C. & Fiolhais, C. Energy and pressure versus volume: Equations of state motivated by the stabilized jellium model. *Phys. Rev. B* **63**, 224115 (2001).

56. Henkelman, G., Uberuaga, B. P. & Jónsson, H. A climbing image nudged elastic band method for finding saddle points and minimum energy paths. *J. Chem. Phys.* **113**, 9901-9904 (2000).

57. Henkelman, G., Jóhannesson, G. & Jónsson, H. Methods for finding saddle points and minimum energy paths. In: Schwartz, S. D. (ed). *Theoretical Methods in Condensed Phase Chemistry*. Springer Netherlands: Dordrecht, 2002, pp 269-302.

58. Henkelman, G. & Jónsson, H. A dimer method for finding saddle points on high dimensional potential surfaces using only first derivatives. *J. Chem. Phys.* **111**, 7010-7022 (1999).

59. Heyden, A., Bell, A. T. & Keil, F. J. Efficient methods for finding transition states in chemical reactions: Comparison of improved dimer method and partitioned rational function optimization method. *J. Chem. Phys.* **123**, 224101 (2005).

60. Kästner, J. & Sherwood, P. Superlinearly converging dimer method for transition state search. *J. Chem. Phys.* **128**, 014106 (2008).

61. Nørskov, J. K. et al. Origin of the overpotential for oxygen reduction at a fuel-cell cathode. *J. Phys. Chem. B* **108**, 17886-17892 (2004).

62. Bureau, C. & Lécayon, G. On a modeling of voltage-application to metallic electrodes using density functional theory. *J. Chem. Phys.* **106**, 8821-8829 (1997).

63. Letchworth-Weaver, K. & Arias, T. A. Joint density functional theory of the electrode-electrolyte interface: Application to fixed electrode potentials, interfacial capacitances, and potentials of zero charge. *Phys. Rev. B* **86**, 075140 (2012).

64. Duan, Z. & Henkelman, G. Theoretical resolution of the exceptional oxygen reduction activity of Au(100) in alkaline media. *ACS Catal.* **9**, 5567-5573 (2019).

65. Abidi, N., Lim, K. R. G., Seh, Z. W. & Steinmann, S. N. Atomistic modeling of electrocatalysis: Are we there yet? *WIREs Comput. Mol. Sci.* **11**, e1499 (2021).

66. NIST Chemistry WebBook. <https://webbook.nist.gov/cgi/cbook.cgi?ID=C7722841&Mask=10#Solubility> (Accessed December 2021).

67. Vinogradova, O., Krishnamurthy, D., Pande, V. & Viswanathan, V. Quantifying confidence in DFT-predicted surface Pourbaix diagrams of transition-metal electrode–electrolyte interfaces. *Langmuir* **34**, 12259-12269 (2018).

68. Hansen, H. A., Rossmeisl, J. & Nørskov, J. K. Surface Pourbaix diagrams and oxygen reduction activity of Pt, Ag and Ni(111) surfaces studied by DFT. *Phys. Chem. Chem. Phys.* **10**, 3722-3730 (2008).

69. Viswanathan, V., Hansen, H. A., Rossmeisl, J. & Nørskov, J. K. Unifying the $2e^-$ and $4e^-$ reduction of oxygen on metal surfaces. *J. Phys. Chem. Lett.* **3**, 2948-2951 (2012).

70. Kulkarni, A., Siahrostami, S., Patel, A. & Nørskov, J. K. Understanding catalytic activity trends in the oxygen reduction reaction. *Chem. Rev.* **118**, 2302-2312 (2018).

71. Ford, D. C., Nilekar, A. U., Xu, Y. & Mavrikakis, M. Partial and complete reduction of O_2 by hydrogen on transition metal surfaces. *Surf. Sci.* **604**, 1565-1575 (2010).

72. Bhat, K. S., Barshilia, H. C. & Nagaraja, H. S. Porous nickel telluride nanostructures as bifunctional electrocatalyst towards hydrogen and oxygen evolution reaction. *Int. J. Hydrol. Energy* **42**, 24645-24655 (2017).

73. Kolb, E. D. & Laudise, R. A. The solubility of trigonal Se in Na_2S solutions and the hydrothermal growth of Se. *J. Cryst. Growth* **8**, 191-196 (1971).

74. Ravel, B. & Newville, M. ATHENA, ARTEMIS, HEPHAESTUS: data analysis for X-ray absorption spectroscopy using IFEFFIT. *J. Synchrotron Radiat.* **12**, 537-541 (2005).

75. Lu, Z. et al. High-efficiency oxygen reduction to hydrogen peroxide catalysed by oxidized carbon materials. *Nat. Catal.* **1**, 156-162 (2018).

76. Jiang, K. et al. Highly selective oxygen reduction to hydrogen peroxide on transition metal single atom coordination. *Nat. Commun.* **10**, 3997 (2019).